EVOLUTIONARY BIOLOGY

Genetic adaptations of sea anemone to hydrothermal environment

Yang Zhou[1], Helu Liu[1], Chenguang Feng[2], Zaiqing Lu[3], Jun Liu[1], Yanan Huang[1,4], Huanhuan Tang[5], Zehui Xu[1,4], Yujin Pu[1,4], Haibin Zhang[1]*

Hydrothermal vent habitats are characterized by high hydrostatic pressure, darkness, and the continuous release of toxic metal ions into the surrounding environment where sea anemones and other invertebrates thrive. Nevertheless, the understanding of metazoan metal ion tolerances and environmental adaptations remains limited. We assembled a chromosome-level genome for the vent sea anemone, *Alvinactis idsseensis* sp. nov. Comparative genomic analyses revealed gene family expansions and gene innovations in *A. idsseensis* sp. nov. as a response to high concentrations of metal ions. Impressively, the metal tolerance proteins *MTPs* is a unique evolutionary response to the high concentrations of Fe^{2+} and Mn^{2+} present in the environments of these anemones. We also found genes associated with high concentrations of polyunsaturated fatty acids that may respond to high hydrostatic pressure and found sensory and circadian rhythm–regulated genes that were essential for adaptations to darkness. Overall, our results provide insights into metazoan adaptation to metal ions, high pressure, and darkness in hydrothermal vents.

INTRODUCTION

Deep-sea hydrothermal vents are places where seawater heated by hot magma seeps out through fissures in the ocean crust in the vicinity of spreading centers or subduction zones (*1*). When seawater is heated, which can exceed 400°C, the fluids become more acidic, and metals are leached from the surrounding rock. The hydrothermal fluid rises to about 100 to 500 m above the seafloor and spreads laterally in the direction of the dominant ocean current (*2*). Although the deep-sea vent ecosystem is characterized by extreme temperatures and pressures, toxic minerals, and darkness, the creatures that live there flourish and establish a completely unique and intriguing ecosystem. Deep-sea vent habitat is one of the most productive ecosystems on the planet (*3*). Chemosynthetic autotrophs provide vent invertebrates, such as tubeworms, shrimp, and mussels, energy and nutrients without the need for sunlight, and they ultimately support the entire system (*1*, *4*). Meanwhile, deep-sea organisms have developed distinctive physiological and ecological characteristics through long-term adaptive evolution.

Marine invertebrates in coastal areas endure varying levels of dissolved metals and use diverse detoxification mechanisms, including the binding of metallothionein to metal ions, lysosomes in metal ion compartmentalization, and sequestration of metal ion in insoluble granule (*5*, *6*). At deep-sea hydrothermal vents, many dissolved metal ions, which included iron (Fe^{2+}), zinc (Zn^{2+}), manganese (Mn^{2+}), cadmium (Cd^{2+}), cobalt (Co^{2+}), and copper (Cu^{2+}), are carried by the high-temperature plumes of vents and settle around them (*4*, *7*). Previous studies have demonstrated that invertebrates residing in proximity to hydrothermal vents accumulate enormous amounts of metal ions within their diverse tissues (*8*, *9*), but they exhibit no visible signs of stress or malformations (*10*). This suggests the potential presence of specialized metal ion detoxification strategies in these organisms. High hydrostatic pressure is another challenge to deep-sea vent species, and this pressure increases with depth. It is generally known that high hydrostatic pressure can reduce the fluidity and transport function of cell membranes while also affecting most protein folding and activity (*11*). Notably, deep-sea invertebrates exhibit parallel evolutionary in membrane lipids and cholesterol metabolism, possibly as an adaptation to high hydrostatic pressure (*12*, *13*). Furthermore, sunlight is entirely absent below 1000-m depth, but vent invertebrates could perceive light (*14*, *15*). The canonical circadian clock genes have been identified in vent mussels, suggesting the potential presence of biological rhythms (*15*). However, the limited genomic data of vent-associated organisms hindered our capacity to gain further insights into how to adapt to these extreme conditions, especially concerning metal ion.

Hydrothermal vent fields on the Central Indian Ridge (CIR) are spaced discretely >1000 km apart along the ridge axis (*16*). According to the spatial distribution of vent species in the vent field, the typical vent area on the CIR is divided into six areas, among which the central Kairei and Edmond vent fields have high genetic and geological connectivity (*17*). The Edmond vent field is dominated by old, disaggregated sulfide structures, peripheral relict black-smoker chimneys, and massive sulfide talus, and the Edmond fluids have hotter brines than other vents (*18*). Moreover, several transition metals (i.e., Fe^{2+}, Mn^{2+}, Cu^{2+}, Zn^{2+}, Cd^{2+}, and Pb^{2+}) are enriched in the Edmond vent fluid at levels much higher than those of ambient seawater. Notably, Fe^{2+} concentrations are exceptionally high compared with the global dataset (*18*). Sea anemones are an essential taxon of cnidarian that flourish in a variety of deep-sea environments. Most sea anemones thriving in sulfide-rich hydrothermal vent peripheral zone (ambient temperature, 1° to 2°C) obtain nutrients by eating blind shrimp, rather than relying on chemoautotrophic carbon production (*19*). Only one species of the deep-sea hydrothermal vent sea anemone, *Ostiactis*

[1]Institute of Deep-sea Science and Engineering, Chinese Academy of Sciences, Sanya 572000, China. [2]School of Ecology and Environment, Northwestern Polytechnical University, Xi'an 710129, China. [3]Key Laboratory of Mariculture, Ministry of Education, Ocean University of China, Qingdao 266003, China. [4]University of Chinese Academy of Sciences, Beijing 100049, China. [5]Department of Respiratory Medicine, The First Affiliated Hospital of Hainan Medical University, Haikou, Hainan 570102, China.
*Corresponding author. Email: hzhang@idsse.ac.cn

pearseae, maintains an endosymbiotic relationship with sulfide-oxidizing bacteria (*20*). A recent study conducted by our group investigated the transcriptome of *Alvinactis idsseensis* sp. nov. in the Edmond vent, yielding insights into its adaptations to hydrothermal vents, particularly in the areas of energy metabolism and genetic information processing (*21*). However, no adaptive analyses focusing on metal ion, stress, and dark adaptation have been conducted. Considering the heterogeneity of the transcriptome in different tissues and the limitations in obtaining gene loci, whole genomic resources are required to improve our understanding of adaptation to such a unique environment.

Here, we sequenced the chromosome-level genomes of the deep-sea hydrothermal vent sea anemone *A. idsseensis* sp. nov. and transcriptomics to compare with deep-sea anemone *Paraphelliactis xishaensis* and shallow-water cnidarians. In addition, we also validated the crucial genes involved in metal ion tolerance using metal transport activity experiments. The results provide insight into the molecular mechanisms of metal ion homeostasis and adaptations to high hydrostatic pressure and darkness in deep-sea environments.

RESULTS

Genome assembly and characterization

We used a combination of Oxford Nanopore Technologies (ONT) sequencing, Illumina paired-end sequencing, and Hi-C sequencing to sequence the genome of a single specimen of the deep-sea anemone *A. idsseensis* sp. nov. that was collected from the Edmond hydrothermal vent field (Fig. 1, fig. S1, and tables S2 and S3). We first assembled the *A. idsseensis* sp. nov. genome into 442 contigs, with N50 of 1.7 Mb. Then, we incorporated the Hi-C data to anchor the contigs into 17 pseudo-chromosomes, which resulted in a final genome assembly of 475.8 Mb with N50 of 27.6 Mb (tables S4 and S5 and fig. S6). The genome size of *A. idsseensis* sp. nov. is similar to shallow-water sea anemones (table S5), but it has the highest percentage of repeat content (tables S5 and S6). A Benchmarking Universal Single-Copy Orthologs (BUSCO) assessment of the metazoan orthologous gene set indicated that the genome's completeness was 92.8%, which is comparable to the published sea anemone genomes (table S7). A total of 31,960 protein-coding genes were annotated by combining ab initio gene prediction, homology-based prediction, and transcript method prediction (table S8). Of these, 29,928 (93.6%) were supported by transcriptome evidence, and 28,803 (90.12%) genes were annotated using public databases (table S8). Furthermore, the GC content, codon usage, gene length, and exon number of *A. idsseensis* sp. nov. were similar to shallow-water sea anemones (figs. S7 to S10). Repeat sequences play a key role in genome size, chromosomal rearrangements and construction, and gene regulation (*22*). The genome of *A. idsseensis* sp. nov. has a relatively high repeat content (303 Mb of repeated sequences accounted for 63.27% of the genome; fig. S11 and table S6). This proportion is higher than in other genomes of sea anemones (table S5). DNA transposons accounted for about 18.6% of the genome, followed by long terminal repeats (LTRs) at 4.02% and long interspersed nuclear elements (LINEs) at 2.80%, but a major proportion of repetitive sequences were previously undescribed (fig. S11 and table S9).

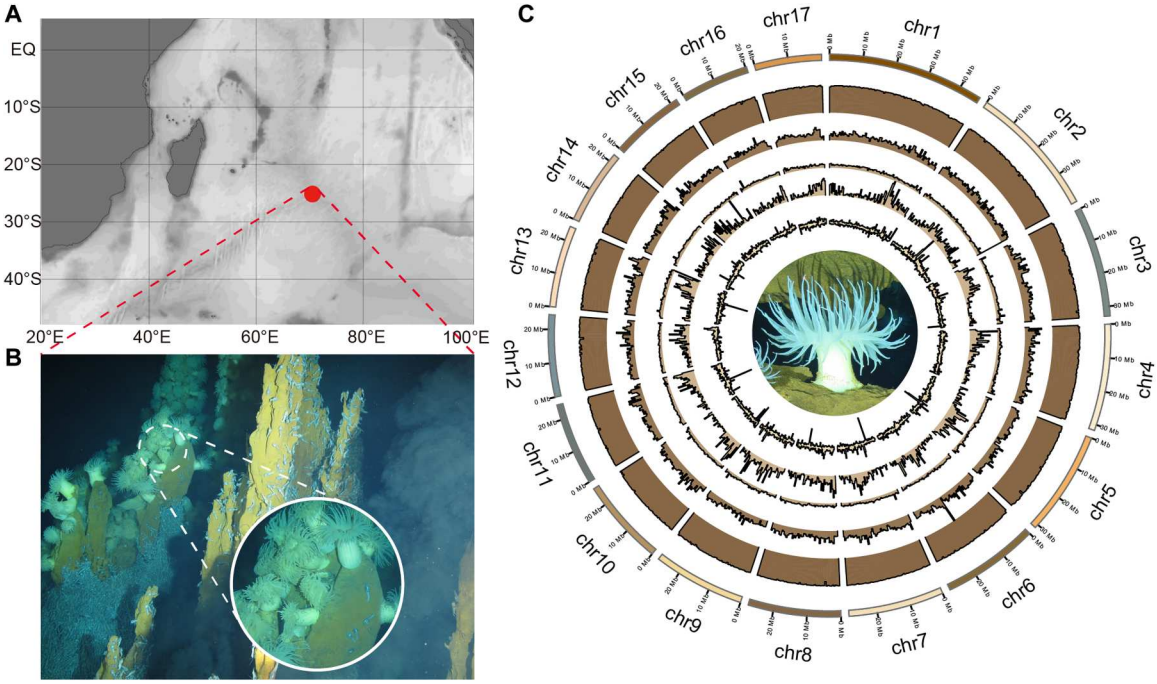

Fig. 1. Sampling information and genome landscape of the deep-sea anemone *A. idsseensis* sp. nov. (**A**) The map shows that the Edmond hydrothermal vent field sampling site is in the mid-ocean ridge of the Southwest Indian Ocean. (**B**) A typical scene is characterized by sea anemones (*A. idsseensis* sp. nov.) and blind shrimp (*R. kairei*) swarming aggregations in the Edmond vent field. *A. idsseensis* sp. nov. thrives on the yellow sulfide layer in the middle and lower regions of the chimney exterior. Rights reserved by IDSSE Deep-sea Scientific Research Image and Video Database. (**C**) Circos plots of the 17 pseudo-chromosomal linkage groups are shown in a circular representation on the outer layer of colored blocks. From outer to inner circles: 500,000 window-based sequencing depth, gene density, GC content percentage, LTR, LINE, and SINE, respectively.

Chromosome-level genome assembly provides a new perspective on the origins and evolution of chromosomes (*23*). Here, macrosynteny comparisons showed high karyotype conservation between the *A. idsseensis* sp. nov. and other sea anemones, but there are interchromosomal rearrangements (Fig. 2B and fig. S12). Overall, we obtained the high-quality chromosome-scale assembly genome of a deep-sea anemone.

Phylogeny, demographic history, and homeobox gene clusters

To verify the phylogenetic position of *A. idsseensis* sp. nov. with respect to other cnidarians, we used the 18 selected datasets of cnidarian genomes to perform phylogenomic analysis. First, we obtained 318 and 348 single-copy orthologous groups using OrthoFinder (*24*) and Reciprocal Best BLAST Hits (RBH) for downstream analysis, respectively. The two datasets gave high-confidence identical topologies, which was consistent with previous molecular phylogenies (fig. S14) (*25*, *26*). The *A. idsseensis* sp. nov. was placed within Metridioidea as a sister to the deep-sea abyssal anemone *P. xishaensis* (Fig. 2A).

At the Edmond hydrothermal vent field, a typical scene consists of large swarms of the blind shrimp *Rimicaris kairei* and aggregations of the sea anemone *A. idsseensis* sp. nov. (*27*). Then, we estimated the dynamic effective population size (*Ne*) of *A. idsseensis* sp. nov., which suggested that the population of *A. idsseensis* sp. nov. underwent a notable population expansion about 80,000 years ago and then stabilized (fig. S15). Although there has been little investigation of the geological histories of the Edmond hydrothermal vent, there is a Kairei hydrothermal vent nearby that is highly correlated with it (*16*). Dating of massive sulfide, sulfide chimney, and mineralized rock breccia samples collected from the Kairei hydrothermal field indicated four episodes of hydrothermal activity (EHA) I to IV that ranged from 8.4 to 96.3 ka. Among them, EHA I is the oldest, and it probably represents the onset of the hydrothermal activity of the field (*28*). Therefore, we speculate that the population of *A. idsseensis* sp. nov. was related to the activity of the chemosynthetic environment.

Hox genes are homeobox transcription factors that play a vital role in the patterning of cnidarian and bilaterian embryos (*29*). *Hox* genes are often found in a cluster, and the position of the genes in the cluster generally corresponds to its temporal and spatial expression (*30*). Therefore, cnidarians are thus vital to our understanding of the *Hox* gene cluster′s early evolution (*29*, *31*). Our analysis revealed that the *A. idsseensis* sp. nov. genome has a *Hox* gene cluster commonly found in sea anemones and Scleractinia, which includes the Hox genes *Anthox6*, *Anthox6a*, *Anthox7*, *Anthox8*, and *Anthox1a*, as well as the extended Hox genes *Rough*, *Gbx*, and *Evx* on chromosome 1 (fig. S13). We conducted a comparative analysis of the *A. idsseensis* sp. nov. *Hox* cluster with published high-quality genomes (contig N50 > 500 kb) of corals and sea anemones. We found that the consistent adjacency genes *Anthox6*, *Evx*, and *Anthox7/8* were present in the ancestral gene cluster of both Scleractinia and Actinaria (*23*, *32*). However, in the *A. idsseensis* sp. nov. lineage, *Anthox6* exhibited a notable separation from Evx and *Anthox7/8*. In addition, we discovered a separate *ParaHox* cluster (*Gsx* and *Xlox/Cdx*) on chromosome 5. This finding is consistent with the presence of a similar cluster in the genome of *Nematostella vectensis* (fig. S13B) (*23*).

Expansion and positive selection of genes linked to vent environment

Comparative analyses among cnidarian genomes (table S5) revealed that 736/31 gene families were significantly expanded/contracted in the *A. idsseensis* sp. nov. genome, respectively (figs. S16 and S17). Gene Ontology (GO) enrichment analysis of the expanded gene families revealed that they were involved mainly in the binding of metal ions (e.g., iron ion binding, ion transport, and heme binding), cell membranes (e.g., integral component of membranes, transmembrane transporter activity, transmembrane transport, and Golgi cisterna membranes), and stress response (e.g., DNA repair and immune response; fig. S18 to S20 and tables S10 and S11).

Simultaneously, we compared the domains of different cnidarians and discovered that the expanded Pfam domain was related primarily to the binding of metal ions (e.g., ZT_dimer and Cation_efflux) and transport (Translin; table S12). In addition, we calculated the distribution of the Ka/Ks ratios in protein-coding genes and found that *A. idsseensis* sp. nov. had the highest Ka/Ks ratio distribution (fig. S21 and table S13). This suggested that coding genes of *A. idsseensis* sp. nov. experienced stronger positive selection pressure than those of other species of sea anemones. From selection test of orthologs along the species tree, we also identified 53 positively selected genes (PSGs) with *A. idsseensis* sp. nov. as the foreground branch (table S14), which were mainly related to ferrochelatase activity, fumarylacetoacetase activity, sulfate adenylyltransferase (adenosine triphosphate) activity, the heme biosynthetic process, and the checkpoint clamp complex (table S15). These results indicated that genes and gene family innovations contributed to cell ion homeostasis and cell membrane functions of *A. idsseensis* sp. nov.

Unexpected detoxification strategy

In deep-sea hydrothermal vents, high-temperature fluid emerges from "black chimneys" on ridge axes that contains high concentrations of metal ions and sulfides leached from rock (*33*), but high biomass communities consisting of numerous endemic and novel species thrive here (*3*). Moreover, invertebrates accumulate metals in the body that produce excess reactive oxygen species (ROS), which induce antioxidant defense mechanisms (*6*).

How these organisms near the vents respond to high concentrations of metals and sulfide is still poorly understood (*34*). First, the mitochondria sulfide-quinone oxidoreductase (*SQR*) pathway is critical for maintaining H_2S homeostasis in metazoans (*35*). We identified a complete set of *SQR* pathway–related genes in the *A. idsseensis* sp. nov. genome with increased copy numbers of sulfite oxidase and thiol sulfurtransferase compared with those of other cnidarians (fig. S22). Furthermore, although we did not identify the common metallothioneins for heavy metal detoxification in aquatic invertebrates (*36*) in the genome of *A. idsseensis* sp. nov. or in other cnidarian genomes, we found 13 copies of metal tolerance proteins (*MTP*s) in chromosome 13 of the *A. idsseensis* sp. nov. genome and only one copy in other cnidarians. The genomic arrangement of *MTP* genes indicated that they originated independently through tandem duplication events (Fig. 3B and figs. S23 and S24). *MTPs* are involved in the cation diffusion facilitator from the cytoplasm and play an important role in metal tolerance and maintaining metal homeostasis in plants (*37*). Although *MTPs* are found widely in plants and have been investigated regularly in

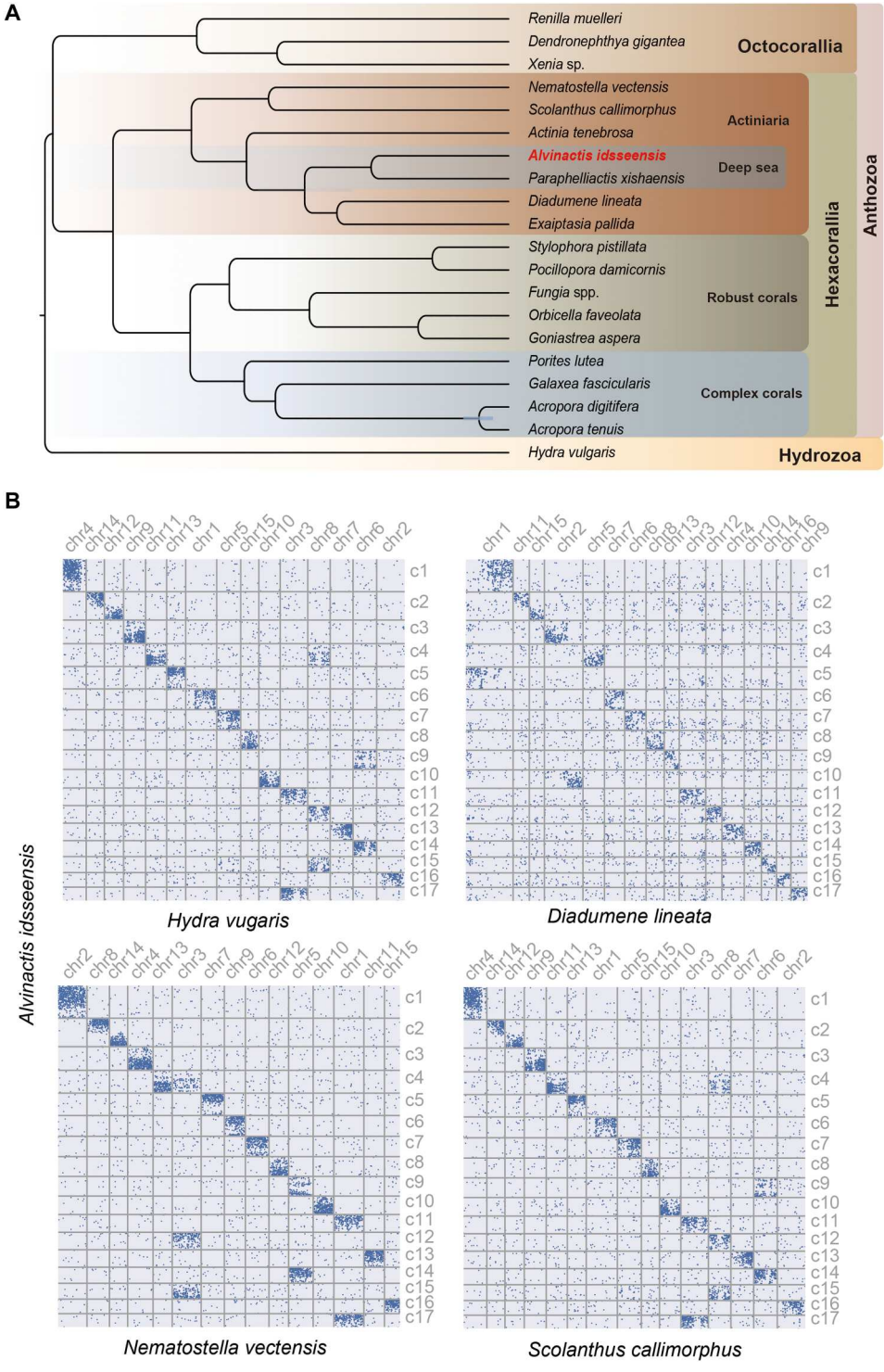

Fig. 2. Evolution of the *A. idsseensis* sp. nov. genome. (**A**) Phylogenetic tree of *A. idsseensis* sp. nov. and selected 19 other Cnidaria taxa based on 216 single-copy orthologs. (**B**) Dot plots showing chromosome-scale macrosynteny comparison between the deep-sea sea anemone *A. idsseensis* sp. nov. and the orange-striped green sea anemone *D. lineata*, the starlet sea anemone *N. vectensis*, the worm sea anemone *S. callimorphus*, and the swiftwater hydra *Hydra vulgaris*. Each dot represents the Reciprocal Best BLAST Hits (RBH) protein between two species.

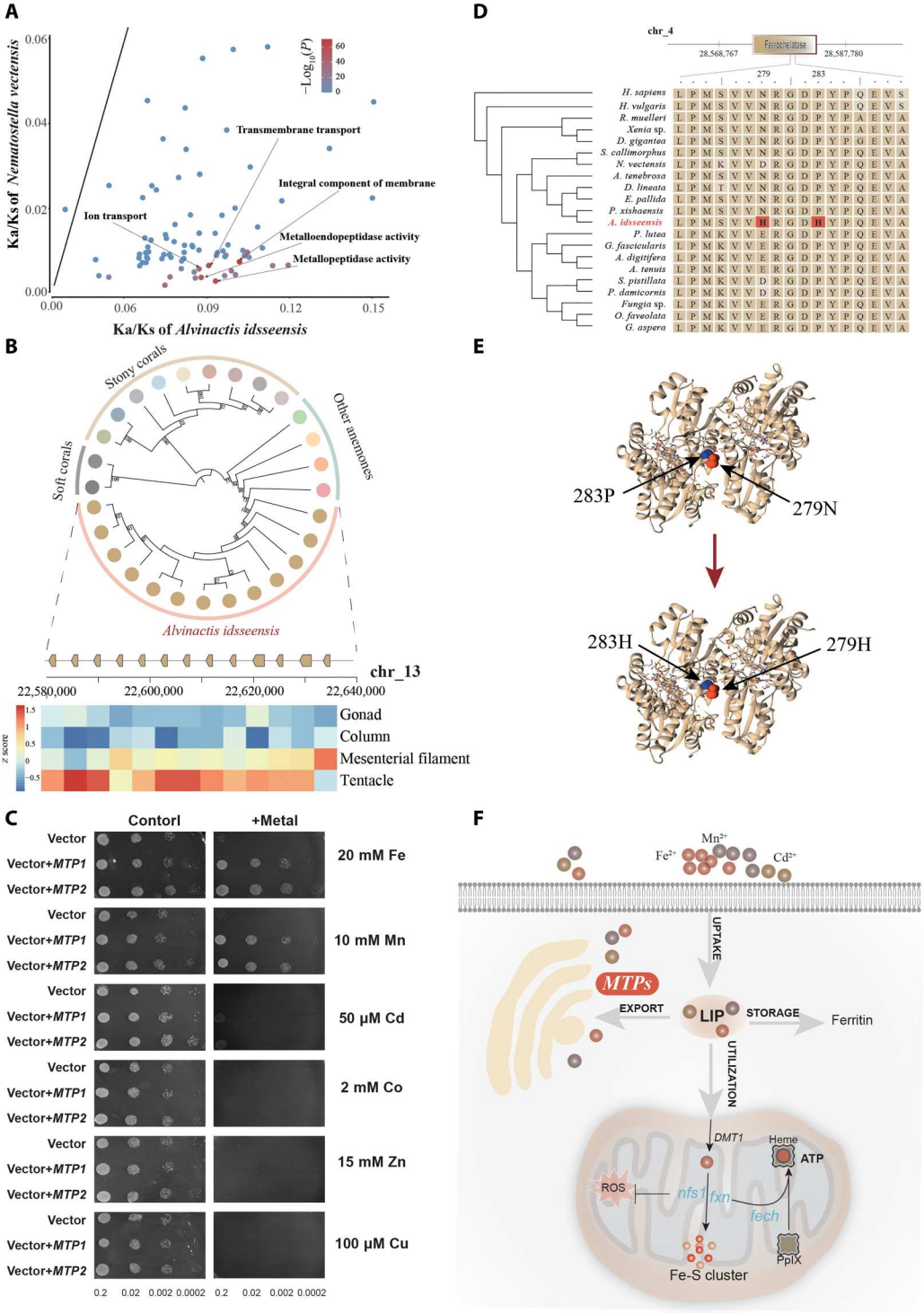

Fig. 3. Adaptation of *A. idsseensis* sp. nov. to tolerance metal ions. (**A**) Rapidly evolving GO categories between *A. idsseensis* sp. nov. and *N. vectensis*. The points represent mean Ka/Ks ratios for two sea anemone genes by GO category. Each point is colored on the basis of the significance (*P* value, one-sided binomial test) of the accumulation in nonsynonymous mutations. (**B**) Phylogenetic analysis of MTP genes, arrangement of MTP gene tandem repeats on the pseudo-chromosome chr13, and their expression patterns in four tissues that include gonad, column, mesenterial filament, and tentacle. The colors on the evolutionary tree represent different species. (**C**) The growth of yeast transformed with the empty vector pYES2.0 or with pYES2.0 that carries *MTPs* in *A. idsseensis* sp. nov. (**D**) Positively selected sites in the conserved regions of *fech* gene. (**E**) Structures adjacent to the substitute sites of the *fech* gene in *A. idsseensis* sp. nov. (**F**) Schematic diagram of the metal adaptation pathway in *A. idsseensis* sp. nov. LIP, labile iron pool; DMT1, divalent metal (ion) transporter 1; PpIX, protoporphyrin IX. Source data are provided as a Source Data file.

plants, they are poorly studied in invertebrates. *MTPs* transport substrates in plants that include divalent cations such as Co^{2+}, Ni^{2+}, Mn^{2+}, Cd^{2+}, Fe^{2+}, and Zn^{2+} (*38*). Multiple copies are also identified in *Arabidopsis*, *Oryza sativa*, *Vitis vinifera*, and other plants, and they are engaged in transport of different metals (*39*, *40*).

To better understand the function and expression pattern of *MTPs*, we analyzed tissue transcriptomes and found that most of the *MTP* genes were expressed mainly in the tentacles (Fig. 3B). Then, we selected two highly expressed *MTPs* in *A. idsseensis* sp. nov. tentacles for functional verification in the yeast expression system and found that yeast cells carrying both *MTPs* exhibited similar growth in control medium and in medium with Fe^{2+} and Mn^{2+}. However, the growth of yeast cells carrying either the empty vector or *MTPs* was inhibited in other heavy metal medium. This result demonstrates that the *MTPs* from *A. idsseensis* sp. nov. are specific transporters for Fe^{2+} and Mn^{2+}. Correspondingly, Fe^{2+} and Mn^{2+} concentrations were exceptionally high compared with the global dataset in the Edmond vent filed. Fe^{2+} and Mn^{2+} are essential trace elements in organisms, but accumulation of intracellular iron and manganese reserves can also be toxic to organisms (*41*). Thus, the expansion of *MTP* genes and their expression patterns indicate that they may help sea anemones tolerate the high levels of Fe^{2+} and Mn^{2+} in the hydrothermal vent environment.

Despite the fact that iron is a necessary component of numerous proteins and enzymes in all living organisms that support biological functions like oxygen transport, excessive iron can lead to the production of peroxides and the accumulation of iron, which can promote iron toxicity (*42*). Therefore, maintenance of cellular iron homeostasis is extremely important for the normal molecular function of organisms. Iron uptake, utilization, and storage are regulated mainly in metazoans to assure the availability of an appropriate supply and to prevent toxicity (*42*). Impressively, we detected a positive selection signal in the ferrochelatase (*fech*) gene of *A. idsseensis* sp. nov. and in a mutation (P283H) in the highly conserved ferrochelatase domain (*43*). In addition, we discovered a rapidly evolving site (N279H) close to this mutation site (Fig. 3, D and E, and figs. S25 and S26). *fech* catalyzes the insertion of Fe^{2+} into the porphyrin macrocycle and plays a regulatory role in the heme synthesis pathway (*43*, *44*), although other divalent ions, such as Mn^{2+}, Cd^{2+}, and Pb^{2+}, can also bind to *fech* as competitive inhibitors (*45*). Furthermore, histidine is known to be a principal metal ion complexing site, which has high metal affinity (*46*).

Our analysis demonstrated that the presence of positively selected sites and rapidly evolving sites for the *fech* gene in the *A. idsseensis* sp. nov. genome increased the binding capacity of iron or other metal ions to be used or detoxified. We also found positive selection signal for cysteine desulfurase, mitochondrial (*nfs1*), and frataxin (*fxn*), which are associated with iron-sulfur (Fe-S) protein synthesis (Fig. 3F and table S14). *nfs1* is an essential maturation of Fe-S proteins in mitochondria, performs the role of a sulfur donor during biogenesis, and is important for regulating iron homeostasis (*47*). Furthermore, *nfs1* helps maintain iron-sulfur cofactors and protect cells from undergoing ferroptosis in response to oxidative damage (*48*). *fxn*, which is an essential mitochondrial iron-sensor protein, acts as a regulator of the Fe-S cluster formation to fine-tune the quantity of Fe-S clusters generated to the concentration of available receptors (*49*).

Overexpression of *fxn* in the mitochondria increases antioxidant capacity and resistance to cellular damage caused by oxidative stress (*50*). Recent studies have confirmed that the main endogenous interactors of *fxn* are *ISCU*, *nfs1*, and *ISD11*, which are components of the core Fe-S assembly complex (*51*), and *fxn* has been characterized as an iron chaperone for *fech* to provide the protein′s ability to heme during biosynthesis (*44*). In total, these coordinated genes may be important in the maintenance of homeostasis of cellular metal ions in deep-sea hydrothermal vent anemones.

Responses to high hydrostatic pressure

Cell division processes, protein stability, DNA structure, and cytoskeletons are also affected by high hydrostatic pressure (*52*). In this study, we found that multiple genes (*dnajb11*, *ttl1*, and *rnfs*) related to mitosis and DNA repair and protein stability were identified as PSGs in the *A. idsseensis* sp. nov. genome (table S14). In addition to this, the condensin II complex subunit H2 (*ncaph2*) gene cluster has undergone lineage-specific expansion in the *A. idsseensis* sp. nov. genome and through tandem duplication (fig. S27), with only one or two copies present in each of the other cnidarian genomes. *ncaph2* increases sister chromatid tension and plays a role in meiosis of homologous chromosomes (*53*). Moreover, we found that 22 gene families were coexpanded significantly in deep-sea anemones (Fig. 4A), and GO enrichment analysis on these expanded gene families revealed that it was related to DNA repair (e.g., DNA repair, DNA integration, DNA recombination, DNA binding, and DNA helicase activity) and membranes (e.g., integral component of membranes and proteolysis; table S16). Thus, the expansion and positive selection of genes may help deep-sea anemones overcome these challenges caused by the high pressure.

Deep-sea hydrostatic pressure increases with depth, and high hydrostatic pressure causes changes in the fatty acid (FA) composition of cell membranes (*54*). Higher hydrostatic pressure causes organisms to produce large amounts of unsaturated FAs (UFA) (*54*), which implies an adaptive strategy to maintain normal membrane structure and function in deeper-sea species (*55*). Here, we determined lipids from the deep-sea hydrothermal vent anemone *A. idsseensis* sp. nov. and shallow-water sea anemone *Phlyctenanthus* sp. Total lipid content of *A. idsseensis* sp. nov. was significantly higher than that of *Phlyctenanthus* sp. [one-way analysis of variance (ANOVA) test, $P = 0.01$; Fig. 4C], and *A. idsseensis* sp. nov. had greater levels of polyunsaturated FAs (PUFAs; one-way ANOVA test, $P = 0.003$; Fig. 4D and table S17). These results indicated that PUFA played a more important role in deep-sea organisms.

Consistent with the results above, we identified expansions in two gene families (i.e., FA synthase, *fasn*, and polyenoic FA isomerase, *pfi*) associated with the FA metabolism pathway in the *A. idsseensis* sp. nov. genome (Fig. 4E and figs. S28 and S29). *fasn* is a single, homodimeric, multifunctional enzyme that catalyzes the synthesis of long-chain saturated FAs with acetyl–coenzyme A (CoA) and malonyl-CoA (*56*). The expansion of *fasn* has been reported in the Mariana hadal snailfish–*Pseudoliparis swirei* genome, which is the deepest vertebrate living in the ocean (*12*). This finding indicates that the expansion of *fasn* may be a convergent evolutionary mechanism for bioaccumulation of PUFA in deep-sea organisms in response to high hydrostatic pressure. Another gene (*pfi*), which is associated with FA isomerization (*57*) also showed increases in the copy number in the *A. idsseensis* sp. nov. genome. In addition, the PSGs *Rv3720* synthesizes phospholipid cyclopropane FA, which improves cell membrane flexibility. *Rv3720* has been

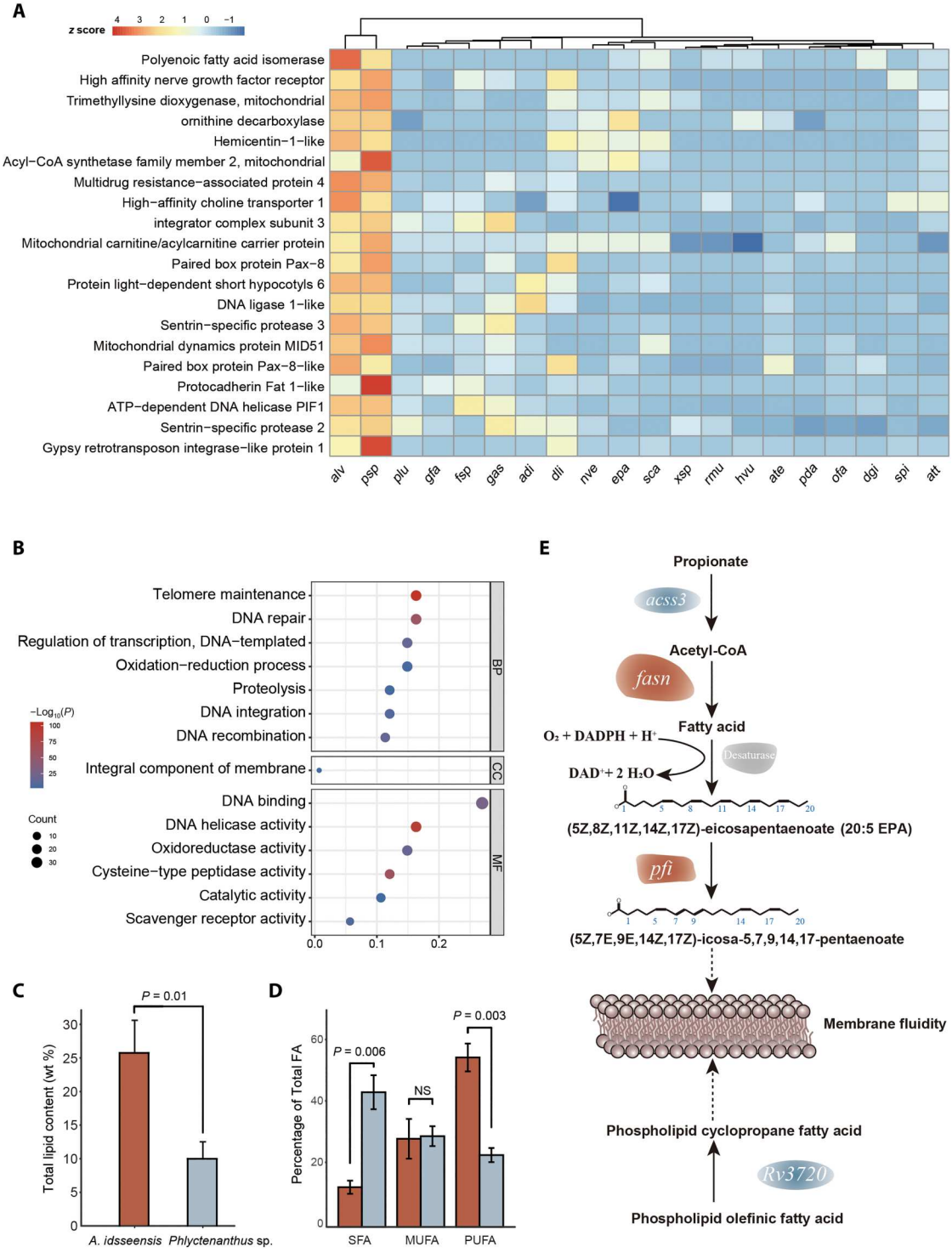

Fig. 4. Deep-sea hydrothermal environmental adaptations. (**A**) Heatmap of the top expanded gene families in two deep-sea anemones and other cnidarians. (**B**) Top 14 enriched GO terms among expansion families in the two deep-sea anemone genomes. (**C**) Total lipid content extracted from the deep-sea hydrothermal vent sea anemone *A. idsseensis* sp. nov. and the shallow-water sea anemone *Phlyctenanthus* sp. Data represent means ± SE from three biological replicates. (**D**) Fatty acid composition for two sea anemones in (A). SFA, saturated fatty acids; MUFA, monosaturated fatty acids. Data represent means ± SE from three biological replicates. (**E**) Membrane fluidity and lipid metabolism–related pathways. *P* value was calculated using one-way ANOVA test. Species code: alv, *A. idsseensis* sp. nov.; adi, *Acropora digitifera*; act, *Acropora tenuis*; plu, *Porites lutea*; gas, *Galaxea fascicularis*; fsp, *Fungia* sp.; gas, *Goniastrea aspera*; pda, *Pocillopora damicornis*; ofa, *Orbicella faveolata*; spi, *Stylophora pistillata*; xsp, *Xenia* sp.; dgi, *Dendronephthya gigantea*; rmu, *Renilla reniformis*; epa, *E. pallida*; nve, *N. vectensis*; sca, *S. callimorphus*; dli, *D. lineata*; ate, *A. tenebrosa*; hvu, *H. vulgaris*.

identified as a rapidly evolving gene in the genome of the deep-sea anemone *P. xishaensis* (*13*). Together, these results show that use of PUFAs to maintain normal cell membrane function may represent an evolutionary convergence by which deep-sea anemone and hadal snailfish respond to high hydrostatic pressure and add to our understanding of the adverse effects high hydrostatic pressure on hydrothermal vent anemones and even deep-sea invertebrates.

Adaptations to darkness

The deep-sea area below 1000 m is defined as an aphotic zone, and sunlight cannot reach that depth. However, it has been confirmed using a charge-coupled device camera that the hydrothermal vents with high temperatures also have a special kind of light source. The hydrothermal vent blind shrimp (*Rimicaris exoculata*) detects thermal radiation from the vent using a novel photoreceptor on its dorsal (*14*), but we do not know how sea anemones sense thermal radiation at close distances to vents.

Opsins are important light-sensitive proteins that support vision and photoreceptors, and they are also involved in sensing temperature and chemicals and participating in circadian rhythms (*58*). Comparative analysis found that there were more copies of GQ-coupled rhodopsin and melanopsin in the deep-sea sea anemone *A. idsseensis* sp. nov. genome (Fig. 5A). These two classes of opsins are scotopic vision proteins that are extremely important for vision in low light conditions (*58*). Moreover, deep-sea anemones are behaviorally more sensitive to long-wavelength blue light and have the ability to bioluminesce (*59*). We might speculate that these opsins may help them detect thermal radiation to prey on blind shrimp in a dark environment.

Recent studies showed that invertebrates that inhabited hydrothermal vents exhibited obvious circadian rhythms and maintained canonical circadian clock genes (*15*). Here, we discovered the core genes of the invertebrate circadian rhythm pathway in the *A. idsseensis* sp. nov. genome. Notably, we found 14 tandem protein cycle genes (*cyc*) on chromosome 9 and only one copy in other cnidarians (Fig. 5B). *cyc* modulates the sleep-wake cycle and the circadian gene regulation by promoting transcription in a negative feedback mechanism (*60*). In addition, α melanocyte–stimulating hormone (melanocyte-stimulating hormone receptor, *MC1R*, and melanocortin 5 receptor, *MC5R*) and melatonin receptor 1A (*MTNR1A*) exhibited an increased copy number in the *A. idsseensis* sp. nov. genome. The melanocyte-stimulating hormone affects the expression of clock genes that are involved in rhythmic processes (*61*), and *MTNR1A* is responsible for circadian rhythm sleep disorders (*62*). Together, we cannot directly determine the existence of a circadian rhythm in the hydrothermal vent anemone *A. idsseensis* sp. nov., but we believe that these changes may help sea anemones retain rhythmic cycles and prey despite living in permanently dark environments (Fig. 5C).

DISCUSSION

Over the past decade, scientists have revealed the symbiotic mechanisms of microorganisms and invertebrates to extreme deep-sea environment (*12*, *13*, *63*, *64*), but few researchers have looked at adaptative mechanisms for metal ions (*8*, *34*). *A. idsseensis* sp. nov. swarms at the Edmond hydrothermal vent field on the CIR, where it is rich in metal ions, especially Fe^{2+} and Mn^{2+} (*18*). In situ video observations found them gathering near hydrothermal vents at a close distance second only to their prey blind shrimp. To thrive in a metal ion–rich environment, *A. idsseensis* sp. nov. has exhibited a certain metal ion tolerance at the genetic level. We found that the *MTP* protein was expanded massively by tandem repeats in the *A. idsseensis* sp. nov. genome. Yeast experiments also demonstrated that these proteins are mainly involved in the transport of Fe^{2+} and Mn^{2+}. *MTP9* was found to be substantially more expressed in the scaly-foot snail *Chrysomallon squamiferum* in the iron-rich Kairei vent field than in the iron-deprived Solitaire vent field (*64*). We believe that *MTPs* are an essential metal tolerance mechanism in the vent organisms, given the unexpectedly high concentrations of Fe^{2+} in the fluid in the Edmond and Kairei hydrothermal vent field. It should also be mentioned that *MTPs* are also expanded in many plants to deal with high concentrations of metal ions in soil (*39*, *40*); we suggest that this may be a specific example of a convergent adaptive mechanism in response to metal tolerance in plants and animals.

Exposure to high concentrations of metal ions can lead to the accumulation of metal ions in sea anemones, which result in oxidative stress (*65*). Here, we found rapid evolution of genes (*fech*, *fxn*, and *nfs1*) involved in metal ion binding and oxidative stress. Note that *fech* catalyzes the insertion of iron ions into protoporphyrin IX, which is essential for iron homeostasis in organisms (*44*). Moreover, the positive selection of *fech*, *fxn*, and *nfs1* promotes the utilization and detoxification of other metal ions and effectively attenuates the adverse effects of oxidative stress (Fig. 3F). The rapid evolution genes related to oxidative stress and the *MTPs* collectively undergo adaptive evolution in *A. idsseensis* sp. nov. as a response to high concentrations of metal ions in the vent environment.

High hydrostatic pressure and darkness are common factors for deep-sea creatures, which affects the fluidity of cell membranes directly, the integrity of DNA strands, and the correct folding of proteins (*52*, *54*). We found that deep-sea anemones have a higher content of lipids than shallow sea anemones, and further analysis found that it was mainly a large quantity of PUFA, which was similar to previous research (*66*). The main factor could be changes in genes associated with FA synthesis in *A. idsseensis* sp. nov. Notably, the expansion of *fasn* was consistent with those found in the hadal snailfish genome, which may be an important evolutionary convergence for marine organisms to adapt to high hydrostatic pressure. Furthermore, we discovered more scotopic vision and circadian rhythm genes in *A. idsseensis* sp. nov., which we believe may aid hydrothermal vent creatures to detect vent locations, capture prey, and adapt to darkness.

In summary, we provide the chromosome-level genome of the sea anemone, *A. idsseensis* sp. nov. to analyze its adaptations to the extreme environment of a hydrothermal vent. Comparative genomics analysis revealed molecular mechanisms of underlying tolerance to metal ions, response to high hydrostatic pressure, and adaptation to darkness. These findings provide valuable insights into the adaptation of invertebrates to extreme deep-sea harsh environments.

MATERIALS AND METHODS

Deep-sea sampling

Between 2018 and 2019, the scientific research vessel "*Tansuo* 1" performed a scientific expedition to the Southwest Indian Ocean

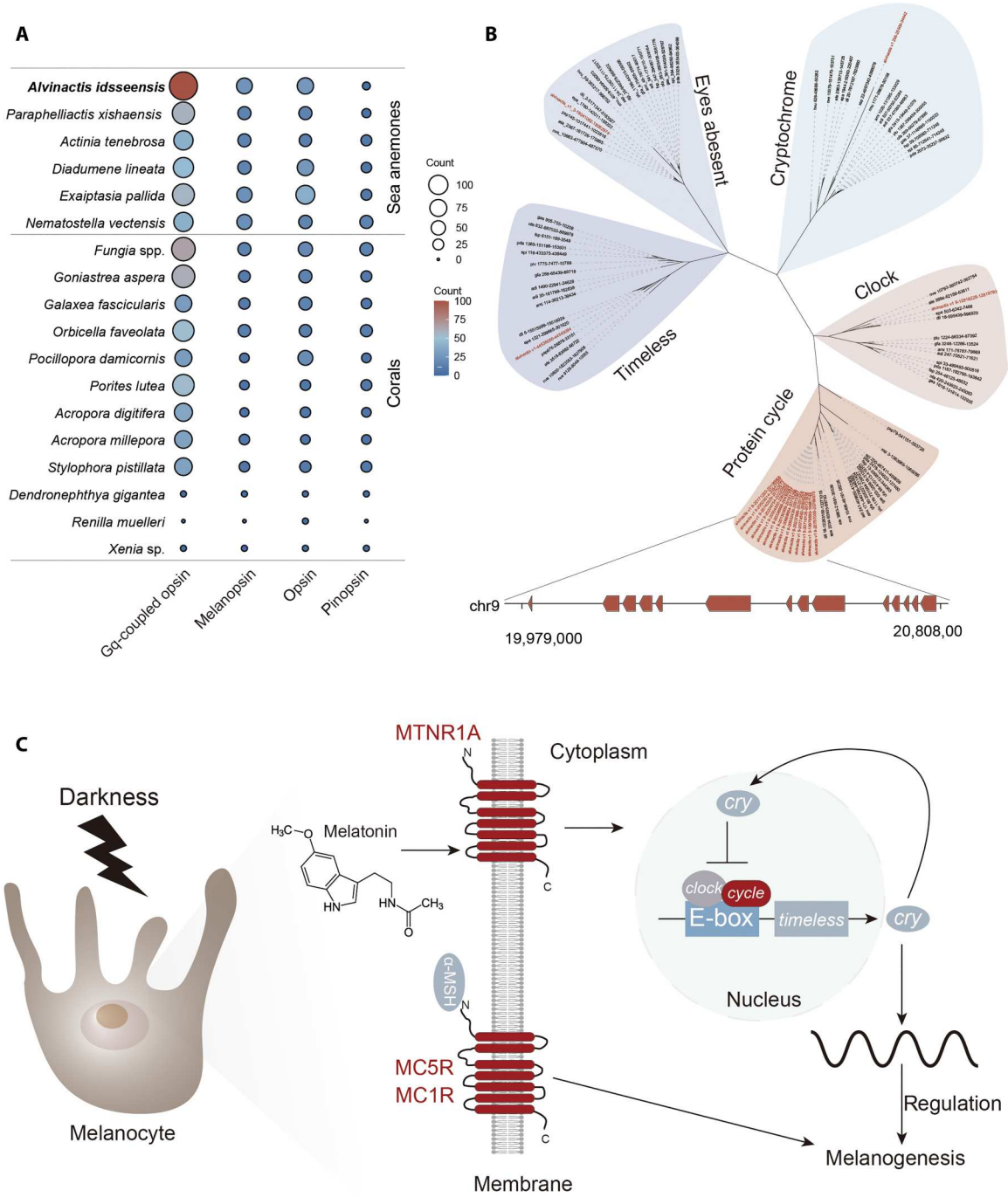

Fig. 5. Photoreceptor and circadian genes in the hydrothermal vent sea anemone *A. idsseensis* sp. nov. (**A**) Gene numbers of opsin in the selected cnidarian genomes. (**B**) Unrooted tree of core rhythm regulate genes in cnidarians. (**C**) Schematic representation of rhythm process of *A. idsseensis* sp. in the vent habitat. Cry, cryptochromes; MC5R, melanocortin 5 receptor; MC1R, melanocyte-stimulating hormone receptor (MSHR), MTNR1A, melatonin receptor type 1A.

hydrothermal region. With the help of the human manned submersible "*Shenhai yongshi*," we found a large population of sea anemones at a hydrothermal vent. Five individuals of the deep-sea anemones *A. idsseensis* sp. nov. were collected from "Edmond" hydrothermal vent filed in the CIR (69 59′E, 23 87′S) at a depth of 3279.1 m using the robotic manipulator (fig. S1). After collecting the samples, they were placed in an insulated biological box and brought to the research vessel. One sample was collected for morphological analysis and preserved in 95% ethanol. The remaining samples were frozen at −80°C refrigerator after arrival of the research vessel *Shenhai Yongshi*. First, the identity of the specimens was confirmed by three mitochondrial genes [12*S* ribosomal DNA (rDNA), 16*S* rDNA, and COIII] and two partial

nuclear genes (18*S* and 28*S* rDNA) and morphology. Detailed information has been described in table S1 and fig. S2.

Genome sequencing and assembly

High–molecular weight genomic DNA was extracted from circular muscle and parietal longitudinal muscle using the QIAGEN Genomic kit (catalog number 13343, QIAGEN, Hilden, Germany) in accordance with the standard protocol provided by the manufacturer. The DNA quality was monitored by using a NanoDrop 2000 spectrophotometer (Thermo Fisher Scientific, USA) and 1% agarose gel electrophoresis. Last, the concentration of DNA was measured using a Qubit Fluorometer v3.0 (Invitrogen, USA).

Paired-end Illumina libraries were constructed using the TruSeq Nano DNA HT Sample Preparation Kit (Illumina USA) following the manufacturer′s protocol, and the libraries were sequenced on the Illumina NovaSeq6000 platform with a paired-end sequencing strategy to obtain ~40.3 Gb of raw data with a read length of 150 base pairs (bp; table S4). For ONT library preparation, the ends of DNA fragments were repaired, and A-ligation reactions were conducted with the NEBNext Ultra II End Repair/dA-tailing Kit (catalog no. E7546, ONT, UK). Following the ligation reaction and quantification, Nanopore sequenced on a Nanopore GridION X5/PromethION sequencer (ONT, UK) instrument on Nextomics (Wuhan, China), yielding a total of ~49.3 Gb of raw data (N50 read length, ~25 kb; fig. S3 and table S4). Illumina and ONT raw reads were preprocessed using Fastp v0.20.0 (*67*) and ontbc v1.1 (https://github.com/FlyPythons/ontbc) with the default settings, respectively.

For Hi-C library construction, First, the samples stored in the −80 refrigerator were thawed at a low temperature, The muscle tissue was separated and added at a rate of 37% formaldehyde to obtain a final concentration of 2% for chromatin cross-linking. After 10 min of induction at room temperature, add 2.5 M glycine to quench the cross-linking reaction. The mixture was then kept on ice for at least 15 min after having already been incubated at room temperature for 5 min. Purified nuclei were digested with 400 U of Mbo I, and biotin-14-dCTP was added afterward. T4 DNA polymerase was used to remove biotin-14-dCTP from unligated DNA ends. Shearing 200- to 600-bp fragments with ligated DNA, end-repair, and purification. Last, the Hi-C libraries were sequenced on the Illumina HiSeq platform. After sequencing, we obtained a total of 262,968,082 paired-end reads of 150 bp from the Illumina HiSeq platform for the Hi-C library.

To begin with genome assembly, genome size estimates for *A. idsseensis* sp. nov. were calculated using KmerFreq_HA program in the SOAPec v2.01 (*68*) on the basis of Illumina filtered raw reads obtained above (fig. S4). NextDenovo v2.4 software (https://github.com/Nextomics/NextDenovo) was used for de novo assembly with ONT proceed data (*69*), followed by three rounds of genome polish with Nextpolish v1.3.1 (*70*), combining Illumina and ONT proceed data with default parameters. Purge_dups v1.0.1 (*71*) using default settings was used to remove haplotigs for the de novo genome. The raw Hi-C reads were trimmed using Fastp v0.20.0 (*67*), and they were aligned to the de novo genome generated from above with the HiC-Pro v2.10 (*72*) pipeline under default settings. All valid reads were used for contig scaffolding using the 3D-DNA pipeline v201008 (*73*) with five rounds of mis-join correction for diploid genomes. The output hic-file and assemblies were checked and manually corrected with Juicebox Desktop v1.11.08 for Windows (*74*). The conserved metazoan gene set "metazoan_odb10" was used to assess the completeness of the final genome assembly and gene models using BUSCO v4.0 (*75*).

For mitochondria genomes, we used clean Illumina short reads to assemble the mitochondrial genomes of *A. idsseensis* sp. nov. using NOVOPlasty v3.7 (*76*). Last, we annotated all features along the sequence using MITOS v2 on Galaxy Europe (*77*) and GeSeq (fig. S5 and table S18) (*78*).

Transcriptomic sequencing and analysis

To obtain gene expression in different tissues, we dissected three individuals′ sea anemone samples for transcriptome sequencing (table S19). Individual sea anemones thawed on ice were dissected for tentacle, column muscle, gonad, and mesenterial filament tissues. Total RNA was extracted using TRIzol (Thermo Fisher Scientific, USA), and RNA quantification and qualification were checked using the NanoPhotometer spectrophotometer (IMPLEN, CA, USA), Qubit RNA Assay Kit in Qubit2.0 Fluorometer (Life Technologies, CA, USA), and RNA Nano 6000 Assay Kit of the Bioanalyzer 2100 system (Agilent Technologies, CA, USA). RNA libraries were generated using NEBNext Ultra RNA Library Prep Kit for Illumina (NEB, USA) following the manufacturer′s protocol and were sequenced by Novogene (Beijing, China) using an Illumina HiSeq platform, and approximately 5 Gb of 150-bp paired-end reads were generated. After the raw reads were filtered with Fastp v0.20.0 (*67*), transcripts were assembled in Trinity v2.8.5 with the following set: --min_contig_length 200 --min_kmer_cov 1. For the gene expression level in each sea anemone tissue, we used HISAT2 v2.2.1 (*79*) to map the filtered reads to the final assembly genome, and fragments per kilobase of exon model per million mapped fragments were calculated by Stringtie v2.1.1 (*80*) for transcript quantification.

Genome gene model prediction and functional annotation

Before gene model prediction, repetitive sequences were annotated using RepeatModeler v2.0.1 (www.repeatmasker.org/RepeatModeler/) and RepeatMasker v4.0.7 (*81*). Tandem repeats were annotated with TRF software v4.0.9 (*82*). The repetitive regions of the sea anemone genome were soft-masked for further gene model prediction. First, Augustus v3.3.3 (*83*) and Glimmerhmm v3.0.4 (*84*) were used for ab initio gene prediction with default parameters. In addition, the protein-coding genes of *N. vectensis* (GCA_932526225.1), *Exaiptasia diaphana* orig.name: *Exaiptasia pallida* (GCA_001417965.1), *Actinia tenebrosa* (GCA_009602425.1), and *Xenia* sp. (GCA_021976095.1) were downloaded from National Center for Biotechnology Information (NCBI) for homology-based gene prediction, and TblastN v2.2.29 was performed to align the soft-masked genome to these gene sets with parameter: -evalue 1e-4. For transcript-based prediction, we first used HISAT2 v2.2.1 (*79*) to align the RNA sequencing proceed reads to the soft-masked genome and then used PASApipeline v2.5.2 (*85*) and Transdecoder v5.5.0 (https://github.com/TransDecoder/TransDecoder) to obtain gene structure information. Last, gene models were generated by combining the ab initio predictions, homology-based gene predictions, and transcript-based predictions using EVidenceModeler v1.1.1 (*86*) with weight

file parameters (TRANSCRIPT:10, PROTEIN:6, and ABINITIO_PREDICTION:1). We annotated the function of the final predicted gene models using BLASTP against NCBI non-redundant (v2020_09), Swiss-Prot (v2020_06), and TrEMBL (v2020_06) with an *E* value cutoff of 1×10^{-5}. GO, Pfam, and KEGG (Kyoto Encyclopedia of Genes and Genomes) were predicted using InterProScan v5.39-77.0 (*87*). The genome landscape plot was generated using Circos v0.69 (*88*) with the sliding window size being 500 kb of the genomes.

Molecular phylogeny and gene family

To determine the phylogenetic position of the *A. idsseensis* sp. nov., we first used 18 Cnidaria protein-coding genes (table S4) to identify the orthologs using the BLAST RBH and implemented in OrthoFinder v2.3.3 (*24*) with the following parameter: -S blast_gz -M msa -I 1.5, respectively. Then, we obtained one-to-one ortholog datasets of 328 genes and 443 genes, respectively. In addition, we also performed a phylogenetic analysis of sea anemones using publicly available transcriptome datasets in conjunction with genomic data (fig. S14 and table S20). Multiple alignments were generated for two protein data matrixes using MUSCLE v3.8.1551 (*89*) under default settings and trimmed by TrimAl v1.4 (*90*) with "-automated1." Phylogenetic tree was reconstructed using maximum likelihood method by RAxML v8.2.12 (*91*) with the following parameters: -m GTRGAMMA -f a -x 12345 -N 100 -p 12345. Species tree was constructed using ASTRAL v5.5.9 (*92*) with default parameters. The expansion and contraction of gene families were analyzed using CAFE v4.2.1 (*93*) with default parameters. Only gene families with a *P* value <0.05 were identified as significantly expanded or contracted. GO and KEGG enrichment of significantly expanded and contracted families were visualized using ggplot2 v3.3.6 package in the R.

Synteny analysis

Macrosyntenic linkages between *Scolanthus callimorphus*, *N. vectensis*, *Diadumene lineata*, and *A. idsseensis* sp. nov. were computed using one-to-one reciprocal best hit. Briefly, we performed NCBI+ BLASTP v2.10 to compare each of the four sea anemone proteomes with an *E* value cutoff of 1×10^{-5}. Then, dot plots were generated using MCScanX (Python version: https://github.com/tanghaibao/jcvi). Macrosynteny relationships plots were generated using NGenomeSyn v1.37 (https://github.com/Hewm2008/NGenomeSyn).

Selection analysis

PSGs were identified using the method described by Chen *et al.* (*94*). Briefly, we first aligned codons sequences of one-to-one homologous genes of the 19 cnidarians by PRANK v170427 (*95*) with parameters: -f = fasta -codon (table S5). Then, Gblocks v0.91b (*96*) were used to extract the conserved regions and removed gaps from alignment coding sequences with default parameters. For PSGs test, we selected *A. idsseensis* sp. nov. as foreground and the other cnidarians in species tree regarded as background. We first tested aBSREL (adaptive branch-site random effects likelihood) model in HyPhy v2.5.23 (*97*) to identify whether foreground branches under positive selection. Only orthologous groups with corrected *P* value <0.05 were retained for downstream analysis. Then, the alternative hypothesis (model = 2, NSsites = 2, fix_omega = 0, omega = 1.5) and the null hypothesis (model = 2, NSsites = 2, fix_omega = 1, omega = 1) for each orthologous group were tested using the Codeml program in PAML v4.9 (*98*). Last, a likelihood ratio test was conducted to compare two hypothesized positive selection sites to be under positive selection on the foreground branch. The *P* values were computed on the basis of chi-square statistics, and genes with a *P* value <0.05 and Bayes probability >90% were treated as PSGs. GO and KEGG enrichment of PSGs are the same as in the "Molecular phylogeny and gene family" section.

Population history of analysis

To estimate historical population size of *A. idsseensis* sp. nov., we used pairwise sequentially Markovian coalescent (PSMC) model (*99*). First, we mapped filtered Illumina reads to the genome of *A. idsseensis* sp. nov. using BWA v 0.7.17 (https://github.com/lh3/bwa) with default parameters. Variable sites were extracted from consensus sequences using bcftools v1.10.2 in samtools v1.9 (*100*) with the following parameters: mpileup -q 20 -Q 20 --ignore-RG. The PSMC analysis consisted of the following parameters: -t 15 -r 5 -p 4+25*2+4+6. Effective population size was calculated using a mutation rate of 3.42×10^{-9} substitutions per site per year, which was estimated by r8s v 1.81 (*101*) with the penalized likelihood method, and the one generation time of the *A. idsseensis* sp. nov. was set to 1 year (*13*).

Phylogenetic identify and analysis of metal tolerance protein

To identify the *MTPs* genes in the *A. idsseensis* sp. nov. genome, we download the Cnidarians homologous *MTPs* sequences from UniProtKB/Swiss-Prot (www.uniprot.org) and GenBank (www.ncbi.nlm.nih.gov/genbank/). Then, these sequences were used as queries to perform TBLASTP in BLAST v2.2.31 searches against the *A. idsseensis* sp. nov. genome with an *E* value threshold of 1×10^{-5}. Candidate *MTPs* genes domains were identified using HMMER v3.1 (*102*) against cation_efflux (PF01545) and ZT dimers hmm file (PF16916) download from Pfam database with an *E* value threshold of 1×10^{-10}. Transmembrane domains were predicted by the TMHMM Server v.2.0 (https://services.healthtech.dtu.dk/service.php?TMHMM-2.0). All *MTPs* sequences were aligned using ClustalX v2.0 (*103*), and a maximum likelihood tree was constructed using IQ-TREE v2.0.6 (*104*) with 1000 bootstrap replicates, and the best substitution model was determined by ModelFinder.

Metal tolerance analysis using yeast expression system

Saccharomyces cerevisiae INVSc1 was recovered in YPD medium (2% polypeptide, 1% yeast extract, and 2% D-glucose). Two highly expressed *MTP* gene (*MTP1* and *MTP2*; table S21) were synthesized in GenScript Company (Nanjing, China) and cloned into pYES2.0 (Invitrogen, Thermo Fisher Scientific Inc.) under the GAL1 promoter. The constructed plasmids were transformed into yeast strains INVSc1. The transformants were selected on uracil-deficient SC (SC-U) plate and precultured in 5 ml of SC-U at 30°C until saturation [optical density at 600 nm (OD_{600nm}) reached a value of 0.6]. Then, cultured yeast cells were diluted with an OD value of 0.02, 0.002, and 0.0002 and transferred to SC-U medium containing 2% (w) Gal, 1% (w/v) raffinose to induce gene expression. The

inducing plates were supplemented with 2 mM $FeSO_4 \cdot H_2O$, 5 mM $MnSO_4$, 15 mM $ZnSO_4$, 100 mM $CuSO_4$, 50 mM $CdCl_2$, or 2 mM $CoCl_2$ to perform metal tolerance analyses according to Li *et al.* (*105*). The empty *pYES2* vector was used as the control. The plates were photographed after 2 days of incubation at 30°C in the dark.

FA analysis using gas chromatography time-of-flight mass spectrometry

To compare the differences in FA content between deep-sea and shallow-water sea anemones, we collected three *Phlyctenanthus* sp. sea anemones from the coast of Hainan Island, China, and comparison with three deep-sea *A. idsseensis* sp. nov. sea anemones. All sea anemone column tissues were dried and weighed separately in a freeze dryer (LC-FD-03H, LICHEN Instrument Technology Co. Ltd., China). Dried samples were chopped, and lipids were extracted using the Folch method. Briefly, each sample was mixed with 24 ml of the Folch solvent ($CHCl_3$:methanol = 2:1, v/v) overnight. Then, the mixture was vortexed for 2 min and centrifuged at 2000 rpm for 10 min. After centrifugation, the same volume of Folch solvent was added to the tissue at room temperature for 2 to 3 hours and centrifuged at 2000 rpm for 5 min to collect the solution. To the solution obtained above, add 0.2 volume of water, vortex for a second, and centrifuge at 2000 rpm for 10 min to obtain a two-phase liquid level. We lastly removed the supernatant and collected the lower layer. Chloroform was dried with N_2 to obtain lipids and weighed. Then the FAME were prepared using Boron fluoride and extracted with n-Hexane.

To analyze total FA composition, lipids extracted in Foch′s solvent were first used for methylation. FA composition of each sample was studied by gas chromatography time-of-flight mass spectrometry (Agilent 8890-LECO Pegasus BT series, MI, USA) with an Rtx-35ms column (30 m, 0.25 mm i.d., 0.10 μm df; Restek, Bellefonte, PA, USA) coupled to a Pegasus III MS system (Leco, St Joseph, MI, USA). The oven temperature was maintained at 50°C for 1 min and then raised to 150°C at 30°C/min. Then, the temperature increased by 2°C/min up to 250°C and lastly to 300°C at 5°C/min. The standard set of the cis/trans produce FA methyl esters (FAME; GLC NESTLE 37 MIX-25MG, Solarbio Science & Technology Co. Ltd., Beijing, China) was used as an external standard for peak evaluation. Individual fatty acids were identified by comparing with commercial standards (Sigma, USA) and quantified with ChemStation program (Agilent Technologies, Palo Alto, USA) (*106*).

Photoreceptor and circadian gene annotation

Photoreceptor and circadian sequences were downloaded from the UniProtKB/Swiss-Prot, and all sequences were used to build a local dataset using BLAST v2.2.31. Then, gene sets from *A. idsseensis* sp. nov. were against local dataset using BLASTX v2.2.31 with following parameters: -evalue 1e-5 -outfmt 0 -num_alignments 5. Gene families were aligned using MAFFT v7.475 (*107*), and the maximum likelihood tree was constructed using IQ-TREE v2.0.6 (*104*) with the best model estimated by ModelFinder.

Supplementary Materials

This PDF file includes:

Supporting Text
Figs. S1 to S29
Tables S1 to S20
Legends for movies S1 and S2
References

Other Supplementary Material for this manuscript includes the following:

Movies S1 and S2

REFERENCES AND NOTES

1. W. Martin, J. Baross, D. Kelley, M. Russell, Hydrothermal vents and the origin of life. *Nat. Rev. Microbiol* **6**, 805–814 (2008).
2. J. Lupton, J. Delaney, H. Johnson, M. Tivey, Entrainment and vertical transport of deep-ocean water by buoyant hydrothermal plumes. *Nature* **316**, 621–623 (1985).
3. V. Tunnicliffe, The biology of hydrothermal vents: Ecology and evolution. *Oceanogr. Mar. Biol.* **29**, 319–407 (1991).
4. C. L. Van Dover, The ecology of deep-sea hydrothermal vents, in *The Ecology of Deep-Sea Hydrothermal Vents* (Princeton Univ. Press, 2021).
5. R. Chiarelli, M. Roccheri, Marine invertebrates as bioindicators of heavy metal pollution. *Open J. Met.* **4**, 93–106 (2014).
6. A. Viarengo, J. Nott, Mechanisms of heavy metal cation homeostasis in marine invertebrates. *Comp. Biochem. Physiol. Part - C: Toxicol. Pharmacol.* **104**, 355–372 (1993).
7. E. Kádár, V. Costa, I. Martins, R. S. Santos, J. J. Powell, Enrichment in trace metals (Al, Mn, Co, Cu, Mo,Cd, Fe, Zn, Pb and Hg) of macro-invertebrate habitats at hydrothermal vents along the Mid-Atlantic Ridge. *Hydrobiologia* **548**, 191–205 (2005).
8. L. Ma, W. X. Wang, Subcellular metal distribution in two deep-sea mollusks: Insight of metal adaptation and detoxification near hydrothermal vents. *Environ. Pollut.* **266**, 115303 (2020).
9. S. Hourdez, D. Jollivet, Metazoan adaptation to deep-sea hydrothermal vents, in *Life in Extreme Environments: Insights in Biological Capability*, A. H. L. Huiskes, G. di Prisco, H. G. M. Edwards, J. Elster, Eds. (Ecological reviews, Cambridge Univ. Press, 2020), pp. 42–67.
10. M. Escobar-Chicho, L. A. Soto, C. Vanegas-Perez, A. Estradas-Romero, Heavy metal bioaccumulation in the anemone *Paraphelliactis pabista* dunn, 1982 (actiniaria: Hormathiidae) from the hydrothermal system of guaymas basin, Gulf of California. *Bull. Environ. Contam. Toxicol.* **102**, 486–491 (2019).
11. P. L. Chong, A. R. Cossins, G. Weber, A differential polarized phase fluorometric study of the effects of high hydrostatic pressure upon the fluidity of cellular membranes. *Biochemistry* **22**, 409–415 (1983).
12. K. Wang, Y. Shen, Y. Yang, X. Gan, G. Liu, K. Hu, Y. Li, Z. Gao, L. Zhu, G. Yan, L. He, X. Shan, L. Yang, S. Lu, H. Zeng, X. Pan, C. Liu, Y. Yuan, C. Feng, W. Xu, C. Zhu, W. Xiao, Y. Dong, W. Wang, Q. Qiu, S. He, Morphology and genome of a snailfish from the mariana trench provide insights into deep-sea adaptation. *Nat. Ecol. Evol.* **3**, 823–833 (2019).
13. C. Feng, R. Liu, W. Xu, Y. Zhou, C. Zhu, J. Liu, B. Wu, Y. Li, Q. Qiu, S. He, W. Wang, H. Zhang, K. Wang, The genome of a new anemone species (Actiniaria: Hormathiidae) provides insights into deep-sea adaptation. *Deep Sea Res. Part I Oceanogr. Res. Pap.* **170**, 103492 (2021).
14. D. G. Pelli, S. C. Chamberlain, The visibility of 350 c black-body radiation by the shrimp *Rimicaris exoculata* and man. *Nature* **337**, 460–461 (1989).
15. A. M. Mat, J. Sarrazin, G. V. Markov, V. Apremont, C. Dubreuil, C. Eche, C. Fabioux, C. Klopp, P. M. Sarradin, A. Tanguy, A. Huvet, M. Matabos, Biological rhythms in the deep-sea hydrothermal mussel *Bathymodiolus azoricus*. *Nat. Commun.* **11**, 3454 (2020).
16. H. Watanabe, G. Beedessee, Vent fauna on the central indian ridge, in *Subseafloor Biosphere Linked to Hydrothermal Systems: Taiga Concept*, J.-i. Ishibashi, K. Okino, M. Sunamura, Eds. (Springer, 2015), pp. 205–212.
17. H. Kumagai, K. Nakamura, T. Toki, T. Morishita, K. Okino, J.-I. Ishibashi, U. Tsunogai, S. Kawagucci, T. Gamo, T. Shibuya, T. Sawaguchi, N. Neo, M. Joshima, T. Sato, K. Takai, Geological background of the Kairei and Edmond hydrothermal fields along the Central Indian Ridge: Implications of their vent fluids′ distinct chemistry. *Geofluids* **8**, 239–251 (2008).
18. R. Gallant, K. Von Damm, Geochemical controls on hydrothermal fluids from the Kairei and Edmond vent fields, 23°–25° s, Central Indian Ridge. *Geochem. Geophys. Geosyst.* **7**, 10.1029/2005GC001067, (2006).
19. C. Van Dover, Trophic relationships among invertebrates at the Kairei hydrothermal vent field (Central Indian Ridge). *Mar. Biol.* **141**, 761–772 (2002).

20. S. K. Goffredi, C. Motooka, D. A. Fike, L. C. Gusmao, E. Tilic, G. W. Rouse, E. Rodriguez, Mixotrophic chemosynthesis in a deep-sea anemone from hydrothermal vents in the Pescadero Basin, Gulf of California. *BMC Biol.* **19**, 8 (2021).
21. Z. Xu, Z. Chen, H. Zhang, Adaptation and evolution of the sea anemone *Alvinactis* sp. To deep-sea hydrothermal vents: A comparison using transcriptomes. *Ecol. Evol.* **12**, e9309 (2022).
22. R. T. Todd, T. D. Wikoff, A. Forche, A. Selmecki, Genome plasticity in Candida albicans is driven by long repeat sequences. *eLife* **8**, (2019).
23. B. Zimmermann, S. M. C. Robb, G. Genikhovich, W. J. Fropf, L. Weilguny, S. He, S. Chen, J. Lovegrove-Walsh, E. M. Hill, C.-Y. Chen, K. Ragkousi, D. Praher, D. Fredman, Y. Moran, M. C. Gibson, U. Technau, Sea anemone genomes reveal ancestral metazoan chromosomal macrosynteny. *biorxiv* 10.1101/2020.10.30.359448, (2022).
24. D. M. Emms, S. Kelly, Orthofinder: Solving fundamental biases in whole genome comparisons dramatically improves orthogroup inference accuracy. *Genome Biol.* **16**, 157 (2015).
25. C. S. McFadden, A. M. Quattrini, M. R. Brugler, P. F. Cowman, L. F. Dueñas, M. V. Kitahara, D. A. Paz-García, J. D. Reimer, E. Rodríguez, Phylogenomics, origin, and diversification of Anthozoans (Phylum Cnidaria). *Syst. Biol.* **70**, 635–647 (2021).
26. A. M. Quattrini, E. Rodríguez, B. C. Faircloth, P. F. Cowman, M. R. Brugler, G. A. Farfan, M. E. Hellberg, M. V. Kitahara, C. L. Morrison, D. A. Paz-García, J. D. Reimer, C. S. McFadden, Palaeoclimate ocean conditions shaped the evolution of corals and their skeletons through deep time. *Nat. Ecol. Evol.* **4**, 1531–1538 (2020).
27. J. Hashimoto, S. Ohta, T. Gamo, H. Chiba, T. Yamaguchi, S. Tsuchida, T. Okudaira, H. Watabe, T. Yamanaka, M. Kitazawa, First hydrothermal vent communities from the Indian Ocean discovered. *Zoolog. Sci.* **18**, 717–721 (2001).
28. Y. Wang, X. Han, X. Jin, Z. Qiu, Z. Ma, H. Yang, Hydrothermal activity events at Kairei field, Central Indian Ridge 25°s. *Resour. Geol.* **62**, 208–214 (2012).
29. T. Q. Dubuc, T. B. Stephenson, A. Q. Rock, M. Q. Martindale, *Hox* and Wnt pattern the primary body axis of an anthozoan cnidarian before gastrulation. *Nat. Commun.* **9**, 2007 (2018).
30. E. Boncinelli, A. Simeone, D. Acampora, M. Gulisano, Homeobox genes in the developing central nervous system. *Ann. Genet.* **36**, 30–37 (1993).
31. U. Technau, G. Genikhovich, Evolution: Directives from sea anemone hox genes. *Curr. Biol.* **28**, R1303–R1305 (2018).
32. T. Q. DuBuc, J. F. Ryan, C. Shinzato, N. Satoh, M. Q. Martindale, Coral comparative genomics reveal expanded *Hox* cluster in the cnidarian–bilaterian ancestor. *Integr. Comp. Biol.* **52**, 835–841 (2012).
33. S. G. Sander, A. Koschinsky, Metal flux from hydrothermal vents increased by organic complexation. *Nat. Geosci.* **4**, 145–150 (2011).
34. L. Zhou, L. Cao, X. Wang, M. Wang, H. Wang, Z. Zhong, Z. Xu, H. Chen, L. Li, M. Li, H. Wang, H. Zhang, C. Lian, Y. Sun, C. Li, Metal adaptation strategies of deep-sea bathymodiolus mussels from a cold seep and three hydrothermal vents in the west pacific. *Sci. Total Environ.* **707**, 136046 (2020).
35. M. Tobler, C. N. Passow, R. Greenway, J. L. Kelley, J. H. Shaw, The evolutionary ecology of animals inhabiting hydrogen sulfide-rich environments. *Annu. Rev. Ecol. Evol. Syst.* **47**, 239–262 (2016).
36. J. C. Amiard, C. Amiard-Triquet, S. Barka, J. Pellerin, P. S. Rainbow, Metallothioneins in aquatic invertebrates: Their role in metal detoxification and their use as biomarkers. *Aquat. Toxicol.* **76**, 160–202 (2006).
37. J. L. Gustin, M. J. Zanis, D. E. Salt, Structure and evolution of the plant cation diffusion facilitator family of ion transporters. *BMC Evol. Biol.* **11**, 76 (2011).
38. F. K. Ricachenevsky, P. K. Menguer, R. A. Sperotto, L. E. Williams, J. P. Fett, Roles of plant metal tolerance proteins (MTP) in metal storage and potential use in biofortification strategies. *Front. Plant Sci.* **4**, 144 (2013).
39. M. Zhang, B. Liu, Identification of a rice metal tolerance protein *OsMTP11* as a manganese transporter. *PLOS ONE* **12**, e0174987 (2017).
40. Z. Shirazi, A. Abedi, M. Kordrostami, D. J. Burritt, M. A. Hossain, Genome-wide identification and characterization of the metal tolerance protein (MTP) family in grape (*Vitis vinifera* L.). *3 Biotech* **9**, 199 (2019).
41. S. Rai, P. K. Singh, S. Mankotia, J. Swain, S. B. Satbhai, Iron homeostasis in plants and its crosstalk with copper, zinc, and manganese. *Plant Stress* **1**, 100008 (2021).
42. M. W. Hentze, M. U. Muckenthaler, B. Galy, C. Camaschella, Two to tango: Regulation of mammalian iron metabolism. *Cell* **142**, 24–38 (2010).
43. S. Al-Karadaghi, M. Hansson, S. Nikonov, B. Jönsson, L. Hederstedt, Crystal structure of ferrochelatase: The terminal enzyme in heme biosynthesis. *Structure* **5**, 1501–1510 (1997).
44. K. Z. Bencze, T. Yoon, C. Millan-Pacheco, P. B. Bradley, N. Pastor, J. A. Cowan, T. L. Stemmler, Human frataxin: Iron and ferrochelatase binding surface. *Chem. Commun.*, 1798–1800 (2007).
45. A. E. Medlock, M. Carter, T. A. Dailey, H. A. Dailey, W. N. Lanzilotta, Product release rather than chelation determines metal specificity for ferrochelatase. *J. Mol. Biol.* **393**, 308–319 (2009).
46. N. G. Nair, G. Perry, M. A. Smith, V. P. Reddy, Nmr studies of zinc, copper, and iron binding to histidine, the principal metal ion complexing site of amyloid-beta peptide. *J. Alzheimers Dis.* **20**, 57–66 (2010).
47. A. Biederbick, O. Stehling, R. Rosser, B. Niggemeyer, Y. Nakai, H. P. Elsasser, R. Lill, Role of human mitochondrial *nfs1* in cytosolic iron-sulfur protein biogenesis and iron regulation. *Mol. Cell. Biol.* **26**, 5675–5687 (2006).
48. S. W. Alvarez, V. O. Sviderskiy, E. M. Terzi, T. Papagiannakopoulos, A. L. Moreira, S. Adams, D. M. Sabatini, K. Birsoy, R. Possemato, *Nfs1* undergoes positive selection in lung tumours and protects cells from ferroptosis. *Nature* **551**, 639–643 (2017).
49. M. A. Huynen, B. Snel, P. Bork, T. J. Gibson, The phylogenetic distribution of frataxin indicates a role in iron-sulfur cluster protein assembly. *Hum. Mol. Genet.* **10**, 2463–2468 (2001).
50. A. P. Runko, A. J. Griswold, K. T. Min, Overexpression of frataxin in the mitochondria increases resistance to oxidative stress and extends lifespan in drosophila. *FEBS Lett.* **582**, 715–719 (2008).
51. S. Schmucker, A. Martelli, F. Colin, A. Page, M. Wattenhofer-Donze, L. Reutenauer, H. Puccio, Mammalian frataxin: An essential function for cellular viability through an interaction with a preformed *iscu/nfs1/isd11* iron-sulfur assembly complex. *PLOS ONE* **6**, e16199 (2011).
52. A. Ishii, T. Sato, M. Wachi, K. Nagai, C. Kato, Effects of high hydrostatic pressure on bacterial cytoskeleton ftsz polymers in vivo and in vitro. *Microbiology* **150**, 1965–1972 (2004).
53. T. D. King, C. J. Leonard, J. C. Cooper, S. Nguyen, E. F. Joyce, N. Phadnis, Recurrent losses and rapid evolution of the condensin ii complex in insects. *Mol. Biol. Evol.* **36**, 2195–2204 (2019).
54. E. F. DeLong, A. A. Yayanos, Adaptation of the membrane lipids of a deep-sea bacterium to changes in hydrostatic pressure. *Science* **228**, 1101–1103 (1985).
55. C. Parzanini, C. C. Parrish, J. F. Hamel, A. Mercier, Functional diversity and nutritional content in a deep-sea faunal assemblage through total lipid, lipid class, and fatty acid analyses. *PLOS ONE* **13**, e0207395 (2018).
56. S. Smith, A. Witkowski, A. K. Joshi, Structural and functional organization of the animal fatty acid synthase. *Prog. Lipid Res.* **42**, 289–317 (2003).
57. A. Liavonchanka, E. Hornung, I. Feussner, M. Rudolph, In-house siras phasing of the polyunsaturated fatty-acid isomerase from propionibacterium acnes. *Acta Crystallogr. F:Struct. Biol.* **62**, 153–156 (2006).
58. A. Terakita, The opsins. *Genome Biol.* **6**, 213–219 (2005).
59. K. Tsutsui, E. Shimada, Y. Tsuruwaka, Deep-sea anemone (Cnidaria: Actiniaria) exhibits a positive behavioural response to blue light. *Mar. Biol. Res.* **11**, 998–1003 (2015).
60. J. E. Rutila, V. Suri, M. Le, W. V. So, M. Rosbash, J. C. Hall, Cycle is a second bhlh-pas clock protein essential for circadian rhythmicity and transcription of drosophila period and timeless. *Cell* **93**, 805–814 (1998).
61. M. N. Moraes, L. R. dos Santos, N. Mezzalira, M. O. Poletini, A. M. Castrucci, Regulation of melanopsins and per1 by α -msh and melatonin in photosensitive xenopus laevis melanophores. *Biomed. Res. Int.* **2014**, 654710 (2014).
62. T. Ebisawa, N. Kajimura, M. Uchiyama, M. Katoh, M. Sekimoto, T. Watanabe, Y. Ozeki, M. Ikeda, T. Jodoi, M. Sugishita, T. Iwase, Y. Kamei, K. Kim, K. Shibui, Y. Kudo, N. Yamada, R. Toyoshima, M. Okawa, K. Takahashi, T. Yamauchi, Alleic variants of human melatonin 1a receptor: Function and prevalence in subjects with circadian rhythm sleep disorders. *Biochem. Biophys. Res. Commun.* **262**, 832–837 (1999).
63. Y. Li, M. G. Tassia, D. S. Waits, V. E. Bogantes, K. T. David, K. M. Halanych, Genomic adaptations to chemosymbiosis in the deep-sea seep-dwelling tubeworm *Lamellibrachia luymesi*. *BMC Biol.* **17**, 91 (2019).
64. J. Sun, C. Chen, N. Miyamoto, R. Li, J. D. Sigwart, T. Xu, Y. Sun, W. C. Wong, J. C. H. Ip, W. Zhang, Y. Lan, D. Bissessur, T. O. Watsuji, H. K. Watanabe, Y. Takaki, K. Ikeo, N. Fujii, K. Yoshitake, J. W. Qiu, K. Takai, P. Y. Qian, The scaly-foot snail genome and implications for the origins of biomineralised armour. *Nat. Commun.* **11**, 1657 (2020).
65. W. P. L. Main, C. Ross, G. K. Bielmyer, Copper accumulation and oxidative stress in the sea anemone, *Aiptasia pallida*, after waterborne copper exposure. *Comp. Biochem. Physiol. Part - C: Toxicol. Pharmacol.* **151**, 216–221 (2010).
66. J. C. Drazen, C. F. Phleger, M. A. Guest, P. D. Nichols, Lipid, sterols and fatty acids of abyssal polychaetes, crustaceans, and a cnidarian from the northeast pacific ocean: Food web implications. *Mar. Ecol. Prog. Ser.* **372**, 157–167 (2008).
67. S. Chen, Y. Zhou, Y. Chen, J. Gu, Fastp: An ultra-fast all-in-one fastq preprocessor. *Bioinformatics* **34**, i884–i890 (2018).
68. R. Luo, B. Liu, Y. Xie, Z. Li, W. Huang, J. Yuan, G. He, Y. Chen, Q. Pan, Y. Liu, J. Tang, G. Wu, H. Zhang, Y. Shi, Y. Liu, C. Yu, B. Wang, Y. Lu, C. Han, D. W. Cheung, S. M. Yiu, S. Peng, Z. Xiaoqian, G. Liu, X. Liao, Y. Li, H. Yang, J. Wang, T. W. Lam, J. Wang, Erratum:

Soapdenovo2: An empirically improved memory-efficient short-read de novo assembler. *Gigascience* **4**, 30 (2015).
69. Y. Zhou, C. Feng, Y. Pu, J. Liu, R. Liu, H. Zhang, The first draft genome of a cold-water coral *Trachythela* sp. (Alcyonacea: Stolonifera: Clavulariidae). *Genome Biol. Evol.* **13**, evaa265 (2021).
70. J. Hu, J. Fan, Z. Sun, S. Liu, Nextpolish: A fast and efficient genome polishing tool for long-read assembly. *Bioinformatics* **36**, 2253–2255 (2020).
71. D. Guan, S. A. McCarthy, J. Wood, K. Howe, Y. Wang, R. Durbin, Identifying and removing haplotypic duplication in primary genome assemblies. *Bioinformatics* **36**, 2896–2898 (2020).
72. N. Servant, N. Varoquaux, B. R. Lajoie, E. Viara, C. J. Chen, J. P. Vert, E. Heard, J. Dekker, E. Barillot, Hic-pro: An optimized and flexible pipeline for hi-c data processing. *Genome Biol.* **16**, 259 (2015).
73. O. Dudchenko, S. S. Batra, A. D. Omer, S. K. Nyquist, M. Hoeger, N. C. Durand, M. S. Shamim, I. Machol, E. S. Lander, A. P. Aiden, E. L. Aiden, De novo assembly of the *Aedes aegypti* genome using hi-c yields chromosome-length scaffolds. *Science* **356**, 92–95 (2017).
74. N. C. Durand, J. T. Robinson, M. S. Shamim, I. Machol, J. P. Mesirov, E. S. Lander, E. L. Aiden, Juicebox provides a visualization system for hi-c contact maps with unlimited zoom. *Cell Syst.* **3**, 99–101 (2016).
75. F. A. Simão, R. M. Waterhouse, P. Ioannidis, E. V. Kriventseva, E. M. Zdobnov, Busco: Assessing genome assembly and annotation completeness with single-copy orthologs. *Bioinformatics* **31**, 3210–3212 (2015).
76. N. Dierckxsens, P. Mardulyn, G. Smits, Novoplasty: De novo assembly of organelle genomes from whole genome data. *Nucleic Acids Res.* **45**, e18 (2017).
77. M. Bernt, A. Donath, F. Juhling, F. Externbrink, C. Florentz, G. Fritzsch, J. Putz, M. Middendorf, P. F. Stadler, Mitos: Improved de novo metazoan mitochondrial genome annotation. *Mol. Phylogen. Evol.* **69**, 313–319 (2013).
78. M. Tillich, P. Lehwark, T. Pellizzer, E. S. Ulbricht-Jones, A. Fischer, R. Bock, S. Greiner, Geseq - versatile and accurate annotation of organelle genomes. *Nucleic Acids Res.* **45**, W6–W11 (2017).
79. D. Kim, J. M. Paggi, C. Park, C. Bennett, S. L. Salzberg, Graph-based genome alignment and genotyping with hisat2 and hisat-genotype. *Nat. Biotechnol.* **37**, 907–915 (2019).
80. M. Pertea, D. Kim, G. M. Pertea, J. T. Leek, S. L. Salzberg, Transcript-level expression analysis of RNA-seq experiments with hisat, stringtie and ballgown. *Nat. Protoc.* **11**, 1650–1667 (2016).
81. N. Chen, Using RepeatMasker to identify repetitive elements in genomic sequences. *Curr. Protoc. Bioinform.* **5**, 4.10.1–4.10.14 (2004).
82. G. Benson, Tandem repeats finder: A program to analyze DNA sequences. *Nucleic Acids Res.* **27**, 573–580 (1999).
83. M. Stanke, S. Waack, Gene prediction with a hidden markov model and a new intron submodel. *Bioinformatics* **19**, ii215–25 (2003).
84. W. H. Majoros, M. Pertea, S. L. Salzberg, Tigrscan and glimmerhmm: Two open source ab initio eukaryotic gene-finders. *Bioinformatics* **20**, 2878–2879 (2004).
85. B. J. Haas, Q. Zeng, M. D. Pearson, C. A. Cuomo, J. R. Wortman, Approaches to fungal genome annotation. *Mycol.* **2**, 118–141 (2011).
86. B. J. Haas, S. L. Salzberg, W. Zhu, M. Pertea, J. E. Allen, J. Orvis, O. White, C. R. Buell, J. R. Wortman, Automated eukaryotic gene structure annotation using evidencemodeler and the program to assemble spliced alignments. *Genome Biol.* **9**, R7 (2008).
87. P. Jones, D. Binns, H. Y. Chang, M. Fraser, W. Li, C. McAnulla, H. McWilliam, J. Maslen, A. Mitchell, G. Nuka, S. Pesseat, A. F. Quinn, A. Sangrador-Vegas, M. Scheremetjew, S. Y. Yong, R. Lopez, S. Hunter, Interproscan 5: Genome-scale protein function classification. *Bioinformatics* **30**, 1236–1240 (2014).
88. M. Krzywinski, J. Schein, I. Birol, J. Connors, R. Gascoyne, D. Horsman, S. J. Jones, M. A. Marra, Circos: An information aesthetic for comparative genomics. *Genome Res.* **19**, 1639–1645 (2009).
89. R. C. Edgar, Muscle: Multiple sequence alignment with high accuracy and high throughput. *Nucleic Acids Res.* **32**, 1792–1797 (2004).
90. S. Capella-Gutierrez, J. M. Silla-Martinez, T. Gabaldon, Trimal: A tool for automated alignment trimming in large-scale phylogenetic analyses. *Bioinformatics* **25**, 1972–1973 (2009).
91. A. Stamatakis, Raxml version 8: A tool for phylogenetic analysis and post-analysis of large phylogenies. *Bioinformatics* **30**, 1312–1313 (2014).
92. C. Zhang, M. Rabiee, E. Sayyari, S. Mirarab, Astral-iii: Polynomial time species tree reconstruction from partially resolved gene trees. *BMC Bioinformatics* **19**, 153 (2018).
93. T. De Bie, N. Cristianini, J. P. Demuth, M. W. Hahn, CAFE: A computational tool for the study of gene family evolution. *Bioinformatics* **22**, 1269–1271 (2006).
94. L. Chen, Q. Qiu, Y. Jiang, K. Wang, Z. Lin, Z. Li, F. Bibi, Y. Yang, J. Wang, W. Nie, W. Su, G. Liu, Q. Li, W. Fu, X. Pan, C. Liu, J. Yang, C. Zhang, Y. Yin, Y. Wang, Y. Zhao, C. Zhang, Z. Wang, Y. Qin, W. Liu, B. Wang, Y. Ren, R. Zhang, Y. Zeng, R. R. da Fonseca, B. Wei, R. Li, W. Wan, R. Zhao, W. Zhu, Y. Wang, S. Duan, Y. Gao, Y. E. Zhang, C. Chen, C. Hvilsom, C. W. Epps, L. G. Chemnick, Y. Dong, S. Mirarab, H. R. Siegismund, O. A. Ryder, M. T. P. Gilbert, H. A. Lewin, G. Zhang, R. Heller, W. Wang, Large-scale ruminant genome sequencing provides insights into their evolution and distinct traits. *Science* **364**, eaav6202 (2019).
95. A. Löytynoja, Phylogeny-aware alignment with prank, in *Multiple Sequence Alignment Methods* (Springer, 2014), pp. 155–170.
96. G. Talavera, J. Castresana, Improvement of phylogenies after removing divergent and ambiguously aligned blocks from protein sequence alignments. *Syst. Biol.* **56**, 564–577 (2007).
97. S. L. Kosakovsky Pond, A. F. Y. Poon, R. Velazquez, S. Weaver, N. L. Hepler, B. Murrell, S. D. Shank, B. R. Magalis, D. Bouvier, A. Nekrutenko, S. Wisotsky, S. J. Spielman, S. D. W. Frost, S. V. Muse, Hyphy 2.5-a customizable platform for evolutionary hypothesis testing using phylogenies. *Mol. Biol. Evol.* **37**, 295–299 (2020).
98. Z. Yang, Paml 4: Phylogenetic analysis by maximum likelihood. *Mol. Biol. Evol.* **24**, 1586–1591 (2007).
99. H. Li, R. Durbin, Inference of human population history from individual whole-genome sequences. *Nature* **475**, 493–496 (2011).
100. H. Li, B. Handsaker, A. Wysoker, T. Fennell, J. Ruan, N. Homer, G. Marth, G. Abecasis, R. Durbin, S., The sequence alignment/map format and samtools. *Bioinformatics* **25**, 2078–2079 (2009).
101. M. J. Sanderson, R8s: Inferring absolute rates of molecular evolution and divergence times in the absence of a molecular clock. *Bioinformatics* **19**, 301–302 (2003).
102. L. S. Johnson, S. R. Eddy, E. Portugaly, Hidden markov model speed heuristic and iterative hmm search procedure. *BMC Bioinformatics* **11**, 431 (2010).
103. M. A. Larkin, G. Blackshields, N. P. Brown, R. Chenna, P. A. McGettigan, H. McWilliam, F. Valentin, I. M. Wallace, A. Wilm, R. Lopez, J. D. Thompson, T. J. Gibson, D. G. Higgins, Clustal w and clustal x version 2.0. *Bioinformatics* **23**, 2947–2948 (2007).
104. L. T. Nguyen, H. A. Schmidt, A. von Haeseler, B. Q. Minh, Iq-tree: A fast and effective stochastic algorithm for estimating maximum-likelihood phylogenies. *Mol. Biol. Evol.* **32**, 268–274 (2015).
105. J. Li, R. Dong, Y. Jia, J. Huang, X. Zou, N. An, J. Song, Z. Chen, Characterization of metal tolerance proteins and functional analysis of *GmMTP8.1* involved in manganese tolerance in soybean. *Front. Plant Sci.* **12**, 683813 (2021).
106. H. Liu, Z. Guo, H. Zheng, S. Wang, Y. Wang, W. Liu, G. Zhang, Functional characterization of a Δ5-like fatty acyl desaturase and its expression during early embryogenesis in the noble scallop chlamys nobilis reeve. *Mol. Biol. Rep.* **41**, 7437–7445 (2014).
107. K. Katoh, K. Misawa, K. Kuma, T. Miyata, Mafft: A novel method for rapid multiple sequence alignment based on fast fourier transform. *Nucleic Acids Res.* **30**, 3059–3066 (2002).
108. E. Rodriguez, M. Daly, Phylogenetic relationships among deep-sea and chemosynthetic sea anemones: Actinoscyphiidae and Actinostolidae (Actiniaria: Mesomyaria). *PLOS ONE* **5**, e10958 (2010).
109. E. Rodriguez, M. Castorani, M. Daly, Morphological phylogeny of the family Actinostolidae (Anthozoa:Actiniaria) with description of a new genus and species of hydrothermal vent sea anemone redefining the family Actinoscyphiidae. *Invertebr. Syst.* **22**, 439–452 (2008).
110. K. A. Zelnio, E. Rodriguez, M. Daly, Hexacorals (Anthozoa: Actiniaria, Zoanthidea) from hydrothermal vents in the South-Western Pacific. *Mar. Biol. Res.* **5**, 547–571 (2009).

Acknowledgments: We acknowledge the crews of the research vessel *Tansuo* 1 and the pilots of the HOV *Shenhai yongshi*. We are grateful to Q. Qiu's laboratory members (especially K. Wang, W. Xu, C. Zhu, B. Wu, Y. Yuan, T. Qin, M. Hu, C. Li, P. Xin, etc.) of the School of Ecology and Environment, Northwestern Polytechnical University, for assistance in bioinformatics analysis. We are grateful to Y. Qu of the Institute of Deep-sea Science and Engineering, Chinese Academy of Science, for assistance with GC-MS detection, and we thank Z. Chen of the Institute of Tropical Crop Genetic Resources, Chinese Academy of Tropical Agricultural Sciences, for the design and advice on yeast experiments. We would like to thank the Institutional Center for Shared Technologies and Facilities of IDSSE, Chinese Academy of Sciences, for the use of their computing resources. We also would like to thank T. A. Gavin, Professor Emeritus, Cornell University, for help with editing this paper. **Funding:** This research is supported by the major scientific and technological projects of Hainan Province to H.Z. (ZDKJ2019011), Strategic Priority Research Program of the Chinese Academy of Sciences to H.Z. (XDA22040502), and The National Key Research and Development Program of China to H.Z. (2016YFC0304905). **Author contributions:** H.Z. and Y.Z. conceived and designed the study. J.L. and H.Z. collected samples. Y.Z., Z.X., and Y.P. prepared the DNA and RNA samples and libraries. Z.X. carried out the draft genome assemblies. Y.Z. carried out Hi-C assembly and analyses, gene predictions, and synteny analyses. Y.Z. and C.F. carried out evolutionary analyses. Y.Z., H.L., and H.Z. designed experiments. Y.Z., Z.L., H.T., and Y.H. performed the yeast experiments. Y.Z. and H.L. performed GC-MS analyses. H.T. collected the shallow-water sea anemone *Phlyctenanthus* sp. Y.Z. and H.Z. drafted the first version of the manuscript. All authors provided comments and approved the manuscript for submission and publication. **Competing interests:** The authors declare that

they have no competing interests. **Data and materials availability:** All data needed to evaluate the conclusions in the paper are present in the paper and/or the Supplementary Materials. All Illumina, Nanopore, and raw transcriptome sequencing reads were deposited into the Sequence Read Archive (under BioProject accession PRJNA909864). The final genome assemblies have been deposited on NCBI GenBank under accession number JAPWCO000000000 and Science Data Bank (ScienceDB) at https://doi.org/10.57760/sciencedb.06919. All the scripts and code of the analysis of this study are available at https://github.com/yangzhou0916/Deep-sea-anemone-genome. Genome assemblies and annotation and repeat elements for the *A. idsseensis* sp. nov. are also available on Zenodo: 10.5281/zenodo.8146501.

Submitted 7 February 2023
Accepted 20 September 2023
Published 20 October 2023
10.1126/sciadv.adh0474